Research Square

Preprints are preliminary reports that have not undergone peer review.
They should not be considered conclusive, used to inform clinical practice,
or referenced by the media as validated information.

Integrated CFD-Quantitative Microbial Risk Assessment analysis of thermal comfort, particle deposition and indirect infection risk in a conference room under different occupancy scenarios

Gennaro Angelo Iacobucci

gennaroangelo.iacobucci@phds.uniparthenope.:

University of Naples “Parthenope”

Reza Hamidi Jahromi

University of Naples “Parthenope”

Armando Di Meglio

Mercatorum University

Nicola Massarotti

University of Naples “Parthenope”

Research Article

Keywords:

Posted Date: November 9th, 2026

DOI: https://doi.org/10.21203/rs.3.rs-11403529/v1

License: This work is licensed under a Creative Commons Attribution 4.0 International License.
Read Full License

Additional Declarations: No competing interests reported.

Integrated CFD-Quantitative Microbial Risk Assessment analysis of thermal comfort, particle deposition and indirect infection risk in a conference room under different occupancy scenarios

Gennaro Angelo Iacobucci[1*], *Reza Hamidi Jahromi*[1], *Armando* Di Meglio[2] and *Nicola Massarotti*[1]

[1]Department of Engineering, University of Naples "Parthenope", Centro Direzionale Isola C4, 80143, Naples, Italy
[2]Department of Engineering and Science, Mercatorum University, Piazza E. Mattei 10, Rome, 00186, Italy

Abstract. Conference rooms experience large and rapid variations in occupancy, which alter internal heat gains and the interaction between supply jets and occupant thermal plumes. This study investigates how occupancy affects thermal comfort, the deposition of exhaled droplets on occupants and the associated indirect (deposition–hand–mucosa) infection-risk indicators in a mechanically ventilated hotel conference room in Naples, Italy. A steady RANS model of the airflow and temperature fields is coupled with one-way Lagrangian tracking of 10 μm droplets released by the speaker, and the predicted deposition on each occupant is used as input to a Quantitative Microbial Risk Assessment (QMRA) chain. The model is verified through grid and time-step sensitivity analyses and validated against benchmark data from the literature. Four occupancy levels are compared: 25%, 50%, full and overfull condition with standing attendees. Increasing occupancy shifts the flow from a jet-dominated to a plume-influenced regime and raises the PMV from about −0.5 at 25% occupancy to +0.41 on average, and up to +0.75 in individual rows, under overfull conditions. In all scenarios, the first row receives the largest share of droplets among seated occupants (3.1–3.7% of the emitted droplets), whereas under overfull conditions the standing row along the [windowless] side receives 10.6%. Under conservative assumptions, the corresponding QMRA indicators reach about 0.44% for the first row and 1.45% for the standing row. The results indicate that deposition-related exposure is governed by the airflow pathways between the source and the main outlet rather than by distance alone, and that occupancy management and ventilation design should jointly consider thermal comfort and deposition hotspots.

1 Introduction

In modern society, humans spend a predominant portion of their lives, estimated at almost 80% and 90%, within indoor environments [1–4]. Consequently, ensuring high Indoor Environmental Quality (IEQ), encompassing thermal comfort, indoor air quality, visual comfort, and acoustic comfort, has become a fundamental requirement in building design and public health protection. Poor indoor environmental conditions are directly associated with discomfort, reduced productivity, and symptoms commonly related to Sick Building Syndrome (SBS), such as headaches, fatigue, dizziness, and nausea [5–13].

* Corresponding author: gennaroangelo.iacobucci@phds.uniparthenope.it

From an engineering perspective, maintaining adequate levels of thermal comfort and indoor air quality represents a particularly complex challenge, as Ventilation and Air Conditioning systems (HVAC) account for a major share of building energy consumption [14–16]. This issue becomes even more critical in densely occupied environments such as conference halls, theatres, seminar rooms, and university classrooms, where occupancy may rapidly vary from a few individuals to more than one hundred occupants. In these spaces, occupants simultaneously act as sources of heat, moisture, carbon dioxide, and potentially contaminating respiratory particles (D'Alicandro et al.; Nada et al.) [17,18]. Therefore, ventilation system design cannot rely solely on energy-efficiency or thermal-comfort requirements but must also consider air distribution effectiveness, contaminant removal, and exposure-related indicators.

Several studies have investigated the role of HVAC configurations in complex indoor environments, including railway cabins, university classrooms, theatres, data center and operating rooms [17–21]. These studies have demonstrated that airflow organization significantly influences thermo-hygrometric comfort, aerosol transport, particle deposition, and contaminant removal efficiency. Environments characterized by high occupancy density and complex geometries represent especially critical scenarios, where the interaction between mechanical ventilation, human thermal sources, and airborne contaminants can generate highly non-uniform airflow patterns. The COVID-19 pandemic further highlighted the importance of ventilation and indoor airflow patterns in controlling airborne transmission within enclosed spaces. Numerous studies have demonstrated that respiratory particles can remain suspended in the air, be transported by ventilation flows, and generate highly non-uniform exposure conditions [22–24]. Although analytical models based on the well-mixed assumption are useful for preliminary assessments, they are unable to capture local airflow structures, recirculation zones, or differences in exposure among individual occupant locations. Massarotti et al. [20] developed and validated a three-dimensional CFD model of a real operating room, highlighting the importance of accurately representing thermal sources and occupants in predicting airflow behavior. For this reason, Computational Fluid Dynamics (CFD) has become one of the most widely adopted tools for analyzing indoor airflow, aerosol dispersion, and spatially resolved exposure indicators.

Recent CFD studies have shown that the distribution of airborne contaminants strongly depends on the adopted ventilation strategy, air-change rate, source location, and occupant configuration. Vita et al. [25] proposed a CFD-based framework for assessing exposure risk in indoor environments, demonstrating that the well-mixed assumption may be inadequate in the presence of strongly non-uniform airflow fields. Similarly, Moeller et al. [26] showed that CFD simulations enable position-specific exposure-risk assessments, while Lee and Rim [22] demonstrated that ventilation strategies, air-change rates, occupant arrangements, and source locations significantly influence the spatial distribution of exposure and that increasing ACH does not always result in a uniform reduction in risk.

Experimental and epidemiological evidence also confirms the fundamental role of ventilation. Ricolfi et al. [27], by analyzing more than 10,000 Italian classrooms, demonstrated that mechanical ventilation significantly reduces SARS-CoV-2 transmission and that ventilation rates exceeding 10 L s^{-1} per student lead to a substantial reduction in relative risk. However, recent CFD studies have shown that ventilation rate alone is insufficient to describe the actual level of protection. In particular, D'Alicandro et al. [17] investigated the transport of droplets emitted by a lecturer in a large university classroom, highlighting the role of human thermal plumes and showing that increasing ACH does not necessarily guarantee improved contaminant removal. Therefore, ventilation rate alone

cannot adequately describe the actual level of protection, since ventilation effectiveness depends on the interaction among supply jets, room geometry, occupant distribution, and thermal plumes generated by human metabolism.

Respiratory activity represents another key factor affecting aerosol transport. Mariam et al. [28] demonstrated through CFD simulations that coughing, sneezing, normal conversation, and loud speaking generate different dispersion patterns depending on emission velocity, particle-size distribution, and ventilation configuration. Their results further showed that the conventional concept of "safe distance" cannot be considered universally valid, since particle transport strongly depends on airflow organization.

In parallel with studies on airborne transport, increasing attention has been devoted to particle deposition on indoor surfaces. Particles transported by airflow may deposit on occupants and frequently touch surfaces, creating potential contamination hotspots. In this context, Quantitative Microbial Risk Assessment (QMRA) represents an established framework for the quantitative evaluation of microbial risk associated with exposure to pathogenic microorganisms, integrating information related to contamination sources, exposure pathways, and dose–response relationships. Traditionally applied in water-quality and food-safety studies, QMRA has progressively been extended to indoor environments and bioaerosol exposure, enabling the quantification of risks associated with inhalation or contact with contaminated particles. According to Carducci et al. [29], QMRA transforms environmental and exposure data into quantitative risk indicators through the four classical stages of hazard identification, exposure assessment, dose–response assessment, and risk characterization. Although inhalation is generally considered the dominant exposure pathway for respiratory pathogens, the analysis of particle deposition and associated QMRA indicators can provide complementary information useful for identifying critical surfaces, supporting ventilation strategies, and optimizing cleaning procedures.

Despite these advances, three aspects remain insufficiently addressed. First, CFD studies on the effect of occupancy have mainly focused on classrooms and lecture halls [17,22,26], whereas multi-purpose conference rooms, characterised by low ceilings, linear ceiling diffusers, a standing speaker and occupancy that may exceed the design capacity with standing attendees, have received limited attention. Second, although D'Alicandro et al. [17] showed that the occupancy rate modifies the thermo-fluid field and droplet transport in a large classroom, the joint effect of occupancy on thermal comfort (PMV) and on the occupant-resolved deposition of exhaled droplets has not been quantified, particularly under over-capacity conditions. Third, CFD-based risk assessments have almost exclusively addressed the inhalation pathway, typically through Wells–Riley-type models [refs]; CFD-predicted deposition fields have rarely been used as input to QMRA dose–response models for the indirect deposition–hand–mucosa pathway [refs, if any]. Consequently, it is unclear whether the occupancy conditions that ensure thermal neutrality also favour or limit the deposition of exhaled droplets on co-occupants.

To address these gaps, this study couples a steady RANS model of a real, mechanically ventilated hotel conference room with one-way Lagrangian tracking of droplets released by the speaker, and uses the predicted occupant-resolved deposition as input to a QMRA chain for the indirect pathway. Four occupancy levels are compared (25%, 50%, full and overfull occupancy with standing attendees). The study addresses three research questions: how does occupancy modify the airflow structure and the PMV in the occupied zone? how does occupancy affect the fate (deposition, escape, airborne fraction) and the spatial distribution of the droplets released by the speaker? how do these deposition patterns translate into QMRA-derived indicators for the indirect pathway, and is there a trade-off with thermal comfort? The main contributions are: (i) a CFD model of a real conference room, verified through grid and Lagrangian time-step sensitivity analyses and validated against benchmark data for airflow,

temperature and droplet dispersion; (ii) a systematic comparison of four occupancy levels, including an over-capacity scenario, in terms of airflow structure, PMV and occupant-resolved deposition; (iii) the coupling of CFD deposition fields with a QMRA dose–response chain, yielding spatially resolved, comparative risk indicators; and (iv) practical indications on occupancy management and ventilation design that jointly consider thermal comfort and deposition hotspots.

2 Methodology

In this study, an Eulerian–Lagrangian approach is adopted to model airflow, heat transfer, and particle transport. The simulations are performed in two stages. First, the continuous phase (air velocity and temperature) is solved using steady Reynolds Averaged Navier Stokes (RANS) equations. Second, particle dispersion and then deposition are computed by time-integrating Lagrangian trajectories on the steady carrier field using one-way coupling (i.e., particles do not affect the airflow). Consequently, particle motion and deposition are transient, while the carrier flow is assumed to be steady. This strategy reduces the computational cost compared to fully coupled unsteady simulations while retaining time-resolved particle fate statistics [30].

2.1 Continuous Phase

The governing equations are derived from the conservation of mass, momentum, and energy for an incompressible, newtonian fluid and are discretized using the finite volume method. Air is assumed to have constant thermophysical properties, while density variations are considered only in the gravitational term through the Boussinesq approximation to account for buoyancy effects.

Turbulent flow is described within the RANS framework, which instantaneous flow variables are decomposed into mean and fluctuating components according to the Reynolds decomposition. Substituting this decomposition into the Navier–Stokes equations and applying time averaging introduces additional Reynolds stress terms representing the effect of turbulence on the mean flow.

Under these assumptions, momentum transport results from the balance between inertial forces, pressure gradients, viscous diffusion, and buoyancy effects generated by temperature differences, while the energy equation describes the convective and diffusive transport of thermal energy within the airflow. The steady RANS formulation provides the mean carrier flow field, and it is particularly suitable for indoor environments where buoyancy-driven thermal plumes dominate airflow structure and contaminant transport [31]:

$$\nabla \cdot (\bar{u}) = 0, \tag{1}$$

$$\rho \cdot (\bar{u} \cdot \nabla \bar{u}) = -\nabla \bar{p} + \mu \nabla^2 \bar{u} - \nabla \cdot (\rho \overline{u'} \overline{u'}) + B, \tag{2}$$

$$\rho c_p (\bar{u} \cdot \nabla \overline{T}) = k \nabla^2 \overline{T}, \tag{3}$$

where $\bar{u}$ (m/s) is the mean velocity, u' (m/s) the fluctuating component, t (s) the time, ρ (kg/m^3) the air density, p (Pa) the pressure, μ (Ns/m^2) the dynamic viscosity, T (K) the temperature, $c_{p.}$ (J/kg·K) the specific heat capacity, and k (W/mK) the thermal conductivity. The term B (N) represents body forces accounting for buoyancy through the Boussinesq approximation. To close the system, it is necessary to introduce a turbulence model. The choice

typically falls on well-established formulations (e.g., k–ε or k–ω models), which provide a good balance between robustness in near-wall regions and sensitivity to recirculation zones commonly observed in ventilated spaces. In the present study, a k–ε standard considering the wall function [32,33], turbulence model is adopted [20]. The transport equations for the turbulent kinetic energy k and its dissipation rate ε are expressed as:

$$\rho(\bar{u} \cdot \nabla k) = \nabla \cdot \left[\left(\mu + \frac{\mu_t}{\sigma_k}\right)\nabla k\right] + G_k + G_b - \rho\varepsilon; \tag{4}$$

$$\rho(\bar{u} \cdot \nabla \varepsilon) = \nabla \cdot \left[\left(\mu + \frac{\mu_t}{\sigma_\varepsilon}\right)\nabla \varepsilon\right] + C_{1\varepsilon}\frac{\varepsilon}{k}(G_k + C_{3\varepsilon}G_b) - C_{2\varepsilon}\rho\frac{\varepsilon^2}{k}; \tag{5}$$

where k (m^2/s^2) is the turbulent kinetic energy, ε (m^2/s^3) is the turbulent dissipation rate, μ_t is the turbulent viscosity, G_k represents the production of turbulent kinetic energy due to mean velocity gradients, G_b represents the contribution of buoyancy to the production or destruction of turbulent kinetic energy, and σ_k, σ_ε, $C_{1\varepsilon}$, $C_{2\varepsilon}$ and $C_{3\varepsilon}$ are empirical model constants.

The system of equations (1)-(15) has been solved in OpenFOAM (v13) using the PIMPLE algorithm. The pressure equation is solved using an Algebraic MultiGrid (AMG) method, which enhances convergence even on large computational grids, while velocity, energy, and turbulence variables are handled by preconditioned iterative solvers.

Convective terms are treated using limited upwind schemes, designed to ensure numerical stability and prevent spurious oscillations in regions characterized by strong convective gradients, such as airflow jets. Gradient and diffusive terms are computed using second-order linear schemes with limiters, a choice that preserves accuracy where mesh resolution allows and properly accounts for non-orthogonality introduced by geometric constraints.

The convergence criteria are defined by monitoring the residuals of all solved variables. A residual threshold of 10^{-6} is imposed for the energy equation, while a threshold of 10^{-5} is adopted for pressure, velocity, and turbulence quantities. In addition, the stabilization of key integral quantities, including volume-averaged temperature and airflow velocity, is verified to ensure that steady-state conditions are reached.

2.2 Discrete Phase, Lagrangian Particle Tracking

The Lagrangian method is employed to track the trajectories of particles emitted from the source. This model is based on the following assumptions.

- One-way coupling as flow only affects the motion of droplets and not the opposite.
- The motion of each droplet is computed independently using a Lagrangian approach under a dilute dispersed phase assumption, where the particle volume fraction remains sufficiently low (typically less than 10^{-6}), allowing particle–particle interactions such as collisions and coagulation to be neglected. Under this one-way coupling regime, droplet motion is influenced by the carrier airflow without significantly altering the mean flow field. This assumption is consistent with respiratory aerosol simulations involving micrometric droplets ($\approx 10\ \mu m$), for which particle loading is extremely low and the momentum exchange between the dispersed and carrier phases is negligible. Once a droplet reaches a surface, it is assumed to deposit and resuspension effects are neglected [33].

- Droplets are modelled as spherical particles with a density of $1\ g/cm^3$, consistent with the common approximation of respiratory droplets as water-based aerosols reported in previous experimental and numerical studies [33]. Although this assumption restricts the analysis to liquid respiratory droplets rather than solid or evaporated particles, it is appropriate for the present investigation, which focuses on short-range transport and spatial infection risk associated with freshly emitted micrometric droplets [34].

The Lagrangian Particle Tracking (LPT) equations are solved for the droplet motion, considering drag and gravity forces, while other forces are neglected according to methodology presented in the study of Van Beest et al. [35]. The motion of each particle is described as follows [30,36]:

$$\frac{dx_d}{dt} = u_d \tag{6}$$

$$m_d \frac{du_d}{dt} = F_D + F_g \tag{7}$$

where m_d (kg) is the droplet mass, u_d (m/s) in the droplet velocity, F_D (N) and F_g (N) are the drag and gravity forces acting on the droplet, respectively, while x_d (m) is the position of the droplet at each instant of time [31].

2.3 Comfort indices

To quantify thermal comfort of occupants, the PMV index has been used, based on Fanger's heat balance equation [37]. This index enables the assessment of thermal comfort in a stable environment using a 7-point scale from -3 (cold) to +3 (hot). The PMV is calculated from the CFD results by incorporating the following variables:

- air temperature (T_a), relative air velocity (u_{ar}), mean radiant temperature (T_r), and water vapor partial pressure (p_a) as environmental parameters;
- Metabolic rate (M), effective mechanical power (W), and clothing insulation (I_{cl}) as occupant parameters.

The equation for PMV is defined as:

$$PMV = (0.303e^{-0.036M} + 0.028)\left\{\begin{array}{c}(M-W) - 3.05\times10^{-3}\times[5733 - 6.99(M-W) - P_a] - \\ 0.42\times[(M-W) - 58.15] - 1.7\times10^{-5}M(5867 - P_a) - \\ 0.0014M(34 - t_a) - 3.96\times10^{-8}f_{c1}\times[(t_{c1}+273)^4 - (\bar{t_r}+273)^4] - f_c h_c(t_{c1} - t_a)\end{array}\right\}. \tag{8}$$

In the present study, the PMV values were calculated using the built-in *comfort* function implemented in OpenFOAM. The calculations were performed assuming 1.0 for clothing 1.2 (met) for metabolic rate, 0 for mechanical power and 60% for the relative humidity according to legislation UNI EN ISO 7730 [37].

2.4 Infection risk

In this work, contact-mediated infection risk (transmission through contaminated objects) is estimated by coupling transient particle tracking results with a Quantitative Microbial Risk Assessment (QMRA) framework describing

the transmission pathway from particle deposition and decay on skin or clothing, to surface-to-hand transfer, following the hand-to-mucosa contact, and finally the dose–response relationship, consistent with QMRA approaches previously applied to the hand–fomite–mucosa route [38]. From Lagrangian simulations, the cumulative number of droplets that deposit on the skin/clothing surface of each occupant j is obtained as $N_{dep,j}$. Assuming a viral concentration in the respiratory fluid C_v (Ribo Nucleic Acid (RNA) copies/mL), the initial deposited RNA load is computed as shown in Eq. (9):

$$L_{0,j} = N_{dep,j}\, C_v\, V_{p,\mathrm{mL}}, \quad V_{p,\mathrm{mL}} = \left(\frac{\pi}{6} d^3\right) \cdot 10^6, \tag{9}$$

where $V_{p,\mathrm{mL}}$ is the volume of a spherical droplet (diameter d in m) expressed in (mL). To represent viral-load variability, order-of-magnitude scenarios are adopted for C_v (low/medium/high): 10^6, 10^8, and 10^{10} copies/mL, consistent with literature values reporting values up to 10^{11} copies/mL[39]. As Reverse Transcription Quantitative Polymerase Chain Reaction (RT-Qpcr) quantifies RNA copies rather than necessarily infectious virus, an RNA-to-infectious conversion factor f_{viab} (RNA to Plaque Forming Units (PFU)-equivalents) is introduced and treated via scenarios, consistent with reported genome/PFU ratios typically in the range 10^3–10^6 (i.e., $f_{viab} \sim 10^{-6}$–10^{-3}) [40]. The infectious load available on the surface is then modeled using first-order decay in Eq. (10):

$$L_j^*(t) = f_{viab}\, L_{0,j}\, e^{-k_s t}, \tag{10}$$

where k_s is the surface inactivation rate (1/h) and $t_{1/2}$ is the half-life, i.e., the time required for the infectious virus quantity on the surface to decrease by 50%. Under first-order decay, the half-life and the inactivation rate are linked by Equation (11):

$$k_s = \ln(2)/t_{1/2}, \tag{11}$$

meaning that after one half-life the remaining fraction is $e^{-k_s t_{1/2}} = 0.5$.

For skin at approximately 36°C, the following assumptions have been considered: $t_{1/2} = 4.1$ h, yielding $k_s = 0.169\ h^{-1}$ based on the study of Pitol et al. [41]. As a consequence, after 30 minutes, the remaining fraction is $e^{-k_s t} \approx 0.92$ transfers to mucosa. The moist, inner lining of some organs and body cavities (such as the nose, mouth, lungs, and stomach) is modeled in two steps: surface to hand efficiency (η_{sh}) and hand to mucosa with efficiency (η_{hm}), including the number of contacts with the contaminated area (n_c) and the number of hand-to-mucosa contacts (n_f) within the considered time period. The microbial dose transferred to the mucous membranes through indirect contact with contaminated surfaces was estimated using a simplified two-stage transfer model. The formulation accounts for the progressive depletion of microbial material during repeated surface-to-hand and hand-to-mucosa contacts. For each contaminated surface (j), the cumulative transferred dose is calculated as Equation (12):

$$D_j(30\ \text{min}) = L_j^*(0.5)[1-(1-\eta_{sh})^{n_c}][1-(1-\eta_{hm})^{n_f}] \quad (12)$$

where $D_j(30\ \text{min})$ represents the cumulative microbial dose transferred to the mucous membranes from surface (j), and $L_j^*(0.5)$ is the microbial load deposited on that surface at 0.5 h.

Regarding the parameter (n_f), empirical observations report about 23 touches/hour to the face, with 44% involving mucous membranes, giving a "medium" value $n_f \approx 5$ mucosa touches in 30 minutes [42]. For transfer efficiencies, experimental studies report substantial surface-to-hand transfer and a fingertip-to-lip transfer of approximately 0.34. Accordingly, reported in the literature. the $\eta_{sh} = 0.30$ and $\eta_{hm} = 0.34$ have been considered [43]. The parameter n_c (contacts with the contaminated clothing/skin area) is treated as a behavioral scenario parameter (uncertainty) and varied in sensitivity analysis, as it is common in QMRA applications for indirect disease [44]. The model assumes two sequential transfer stages: microbial material is first transferred from the contaminated surface to the hand through repeated contacts and is subsequently transferred from the hand to the mucous membranes[45,46] . At each contact, only a fraction of the microbial material remaining in the donor compartment is transferred to the receiving compartment. Transfer efficiencies are assumed constant, and microbial inactivation, additional contamination, and other removal mechanisms during the contact sequence are neglected.

Unlike a linear formulation based on multiplying transfer efficiencies by contact frequencies, the proposed expression accounts for the finite microbial load available for transfer. Consequently, the cumulative dose cannot exceed the initial microbial load on the contaminated surface, ensuring consistency with mass conservation under the stated assumptions. Finally, a QMRA-derived indirect exposure risk indicator is computed using an exponential dose–response model according to Equation (13):

$$P_j = 1 - e^{-rD_j} \quad (13)$$

To calculate r, the exponential dose–response model developed for SARS-CoV by Watanabe et al. [47] has been adopted. The study reports ID_{50} around 280 PFU, where ID_{50} represents the median infectious dose, i.e., the amount of virus required to infect 50% of exposed individuals; therefore:

$$r = \frac{\ln 2}{ID_{50}} = \frac{ln\ 2}{280} = 2.48 \times 10^{-3}\ \ PFU^{-1} \quad (14)$$

where ID_{50} is the median infectious dose (50% infection probability) and PFU represents the concentration of infectious viral particles.

To facilitate comparison and interpretation, probability of the exposure risk P_j is categorized into three risk levels using probability bands previously adopted in infectious-transmission modelling: Low ($P < 0.1\%$), Medium ($0.1\% \leq P < 1\%$), and High ($P \geq 1\%$)[48].

3 Case study

This section introduces the case study examined in this work, featuring a conference room in Naples, Italy. The room has a floor area of approximately 200 m^2 and represents a typical hotel conference space characterized by frequent use and highly variable occupancy levels.

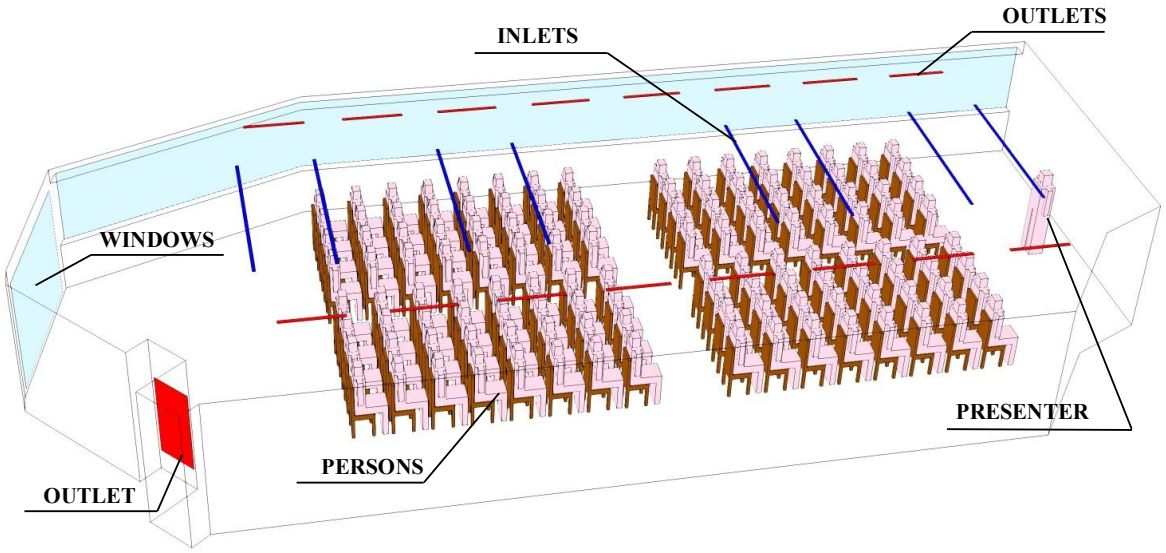


Figure 1.Computational domain of the present study.

3.1 Geometry

The conference room, as depicted in Figure 1, has a length of 22 m, a depth of 10 m, and an internal height of 2.5 m, and is equipped with a mechanically ventilated HVAC system through 8 linear ceiling-mounted supply grilles, each measuring $3.54\,m \times 0.06\,m$ with a supply rate of 0.43 m^3/s. Air extraction is provided by 16 ceiling-mounted exhaust grilles, each with a dimension of $1.18\,m \times 0.08\,m$, uniformly distributed throughout the room to promote effective air removal. In addition, a rectangular exhaust grill with dimensions of $0.8\,m \times 1.6\,m$ is located at one end of the conference room. Additionally, the breathing of individuals inside the room was included to simulate a realistic scenario. To achieve this, the mouths of both the occupants and the presenter were modeled as rectangular surfaces measuring 0.05 m × 0.025 m.

3.2 Boundary conditions

The boundary conditions were specified as follows: the exhalation velocity at the occupants' mouths was set to 0.4 m/s, with a temperature of 36 °C, aligning with body temperature used as boundary condition on the manikins [33]. Regarding the mechanical ventilation system, the inlet air temperature and velocity were fixed at 23 °C and 2 m/s, respectively. The outdoor air temperature was assumed to be 2 °C, representing the winter scenario. Thermal transmittance values of the building envelope were reconstructed based on the actual building characteristics [49–52]. The thermal transmittance values are 0.5 W/m^{2}K for the opaque walls, 0.4 W/m^2K for the ceiling, and 2.0 W/m^2K for the windows. All walls that do not include a window, including the floor, are treated as adiabatic as shown in Figure 1. For the Lagrangian particle-tracking simulations, a sneezing event was

considered as the respiratory emission source. The presenter was selected as the respiratory particle emission source because of their central role during a conference and their position relative to the audience. A single sneezing event was considered as a representative transient respiratory emission scenario to investigate particle transport and deposition under different occupancy conditions. This approach allows the influence of occupancy-induced airflow modifications on particle dispersion to be assessed while maintaining consistent emission conditions across all investigated scenarios. A total of 20,000 particles were injected over a duration of 0.5 s, with an initial velocity of 27 m/s, consistent with values reported in the literature for sneezing events [34]. A monodisperse particle diameter of 10 μm was assumed, representing respiratory droplets that can remain airborne and be transported by indoor airflow. Particle trajectories were computed using a transient Lagrangian approach coupled with the Discrete Random Walk (DRW) model to account for turbulent dispersion. The simulations were performed for a total tracking time of 30 min to evaluate particle transport, deposition patterns on occupants, and the resulting contamination distribution within the conference room. Particle–particle interactions, breakup, coalescence, and evaporation phenomena were neglected, and a one-way coupling approach was adopted due to the relatively low particle concentration.

3.3 Mesh

A three-dimensional computational grid was generated to accurately resolve the temperature and velocity fields within the domain, as shown in Figure 2. The grid was developed using an unstructured discretization with locally refined regions to capture the complex airflow patterns induced by supply jets and occupant-generated thermal plumes. Therefore, targeted mesh refinements were applied near the air supply inlets and outlets, the window surface, and around seated occupants, where more pronounced velocity and thermal gradients are expected. In particular, the refinement around the occupant bodies was designed to properly resolve plume development and jet–plume interaction mechanisms, which play a dominant role in determining local thermal comfort conditions.

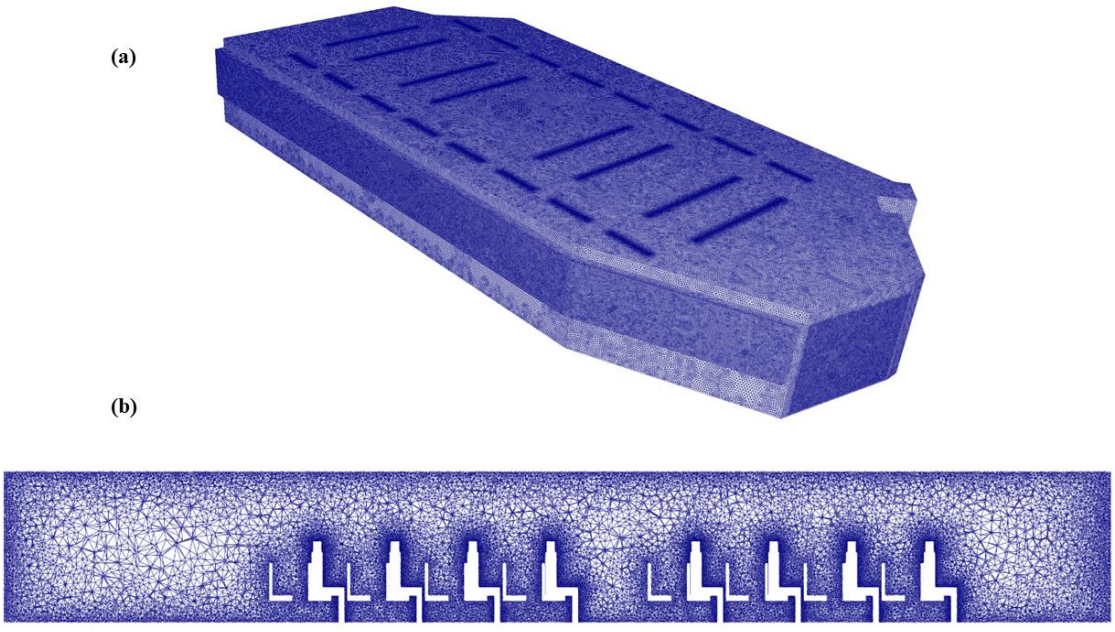


Figure 2. Computational grid visualization (Medium size), 25% occupancy rate. (a) Geometry of the computational domain used for the CFD simulations of the conference room. (b) Longitudinal section of the domain.

4 Verification and validation

This chapter presents the verification and validation of the numerical model. The verification includes the grid independence and Lagrangian time-step sensitivity analyses, while the validation is performed through comparison with experimental data reported in the literature to assess the accuracy and reliability of the numerical predictions.

4.1 Grid sensitivity analysis

For the 25% occupancy rate a grid sensitivity analysis was conducted by comparing temperature and velocity magnitude profiles along three reference lines for coarse, medium, and fine cases. For walls and chairs, the characteristic cell size was reduced from 5.0×10^{-2} m (coarse) to 4.5×10^{-2} m (medium) and 4.0×10^{-2} m (fine). For human bodies and the presenter, the mesh was refined from 2.0×10^{-2} m to 1.5×10^{-2} m and 1.0×10^{-2} m, respectively. A finer resolution was adopted for the mouth region, decreasing from 5.0×10^{-3} m (coarse) to 4.5×10^{-3} m (medium) and 4.0×10^{-3} m (fine), to accurately capture the jet flow and aerosol emission. Similarly, refinement was applied to windows, inlet, and outlet regions, with characteristic cell sizes decreasing from 3.0×10^{-2} m to 2.5×10^{-2} m and 2.0×10^{-2} m.

As a result, the total cell counts increases from 13.487 million for the coarse grid to 20.082 million for the medium grid and 35.261 million for the fine grid. This enables evaluation of grid dependency of the results and helps find a balance between accuracy and computational expense.

As presented in Figure 3, three lines across the domain are considered to compare the velocity and temperature values. Line 3 spans the central region of the room along its longitudinal direction. Line 2 is in the front part of the room, close to the seated occupants, and Line 1 is positioned in the rear part of the room. All lines are at 1.4 m from the floor.

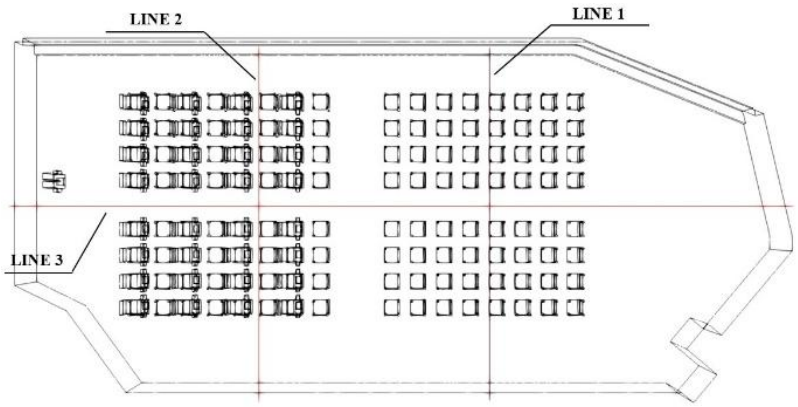


Figure 3. line locations for comparing temperature and velocity fields in a grid sensitivity analysis.

Temperature and velocity profiles obtained along the monitoring lines are presented in Figure 4. In all cases, the temperature profile follows the same trend with local deviation. The coarse grid slightly overpredicts temperature levels, whereas the medium and fine meshes show good agreement in both magnitude and spatial distribution.

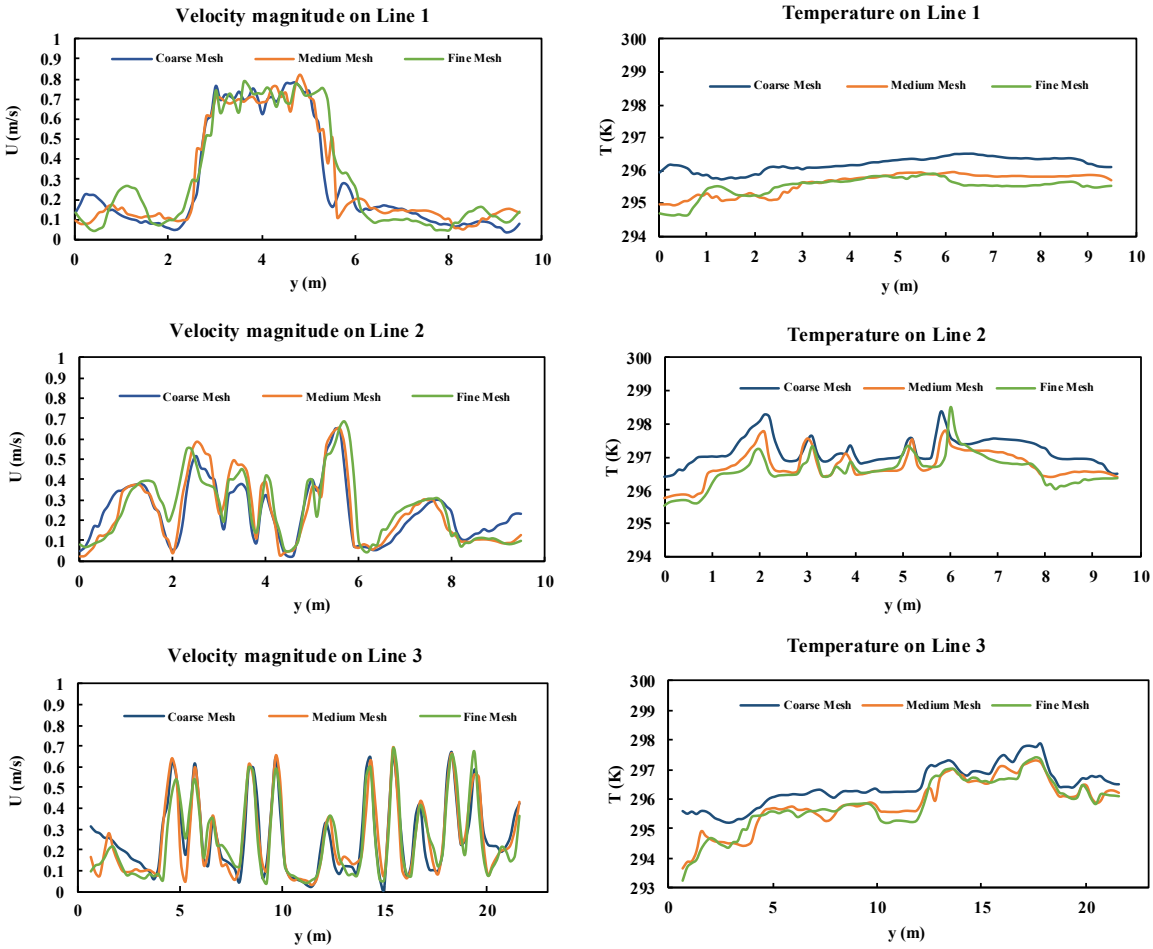


Figure 4.Comparision of temperature and velocity profile for three grids

On the other hand, the coarse grid tends to smooth velocity gradients and underestimate local peaks, whereas the medium and fine meshes show good agreement in both magnitude and spatial distribution. Considering the fine mesh as the most resolved one, the medium mesh is considered sufficient to accurately capture the main airflow difference while ensuring a reasonable computational cost, considering the average error between the coarse and medium grid with the fine one reduces from 2.7 % to 0.4 % and 7.2 % to 2.7% for temperature and velocity values, respectively.The average temperature and velocity values over the lines for the three meshes considered have been reported in Table 1. According to the table, the comparison demonstrates that the velocity and temperature profiles in the medium grid follow the fine-grid solution closely while significantly reducing computational cost. Consequently, the medium mesh was selected for all subsequent simulations.

Table 1.Average velocity and temperature values over the comparison lines, including the errors

Grids	Velocity (m/s)			Temperature (°C)		
	Line 1	Line 2	Line 3	Line 1	Line 2	Line 3
Coarse	0.283	0.238	0.264	23.041	24.022	23.276

Medium	0.292	0.247	0.247	22.484	23.579	22.711
Fine	0.304	0.256	0.245	22.357	23.458	22.663
Differences (Coarse-Fine)	7.2%	7.0%	7.8%	3.1%	2.4%	2.7%
Differences (Medium-Fine)	3.8%	3.3%	0.9%	0.6%	0.5%	0.2%

4.2 Lagrangian time sensitivity Analysis

A time-step sensitivity analysis is performed for the Lagrangian particle tracking using $\Delta t = 0.005$, 0.001 s, and 0.0005 s. The results, as presented in Table 2, show that key particle tracking metrics, namely deposition, escape, and airborne fraction, remain essentially unchanged for a time step $\Delta t \leq 0.001$ s, demonstrating temporal convergence of the Lagrangian solution. Therefore, $\Delta t = 0.001$ s was selected as a suitable compromise between numerical accuracy and computational cost.

Table 2.Results of time-step sensitivity analysis for Lagrangian particle tracking

Δt(s)	**0.005**	**0.001**	**0.0005**
Total stick (%)	48.885	49.685	49.645
Total escape (%)	51.085	50.300	50.330
Total airborne (%)	0.030	0.015	0.025

4.3 Verification and validation

In this section, the verification and validation of the adopted numerical model are presented.

4.3.1 Thermofluid dynamic model

A validation was performed by reproducing the case study by Zhang et al. [32] where the experimental measurements of velocity and temperature were compared and reported in Figure 6 and Figure 7. Three lines, as presented in the Figure 5, have been considered. Temperature is expressed using the dimensionless formulation proposed in ref. [32], $T^* = (T - T_{supply})/(T_{exhaust} - T_{supply})$. The simulated temperature profile correctly reproduces the thermal stratification and the transition height observed in both the reference numerical and the experimental data [32]. The comparison shows good agreement for both trend and the magnitude of the profiles. Local discrepancies are mainly observed close to the supply diffuser and in regions characterized by flow recirculation, where turbulent and mixing effects are more pronounced. These deviations remain limited and do not affect the robustness of the numerical approach, which is therefore deemed reliable and suitable for the subsequent parametric analyses.

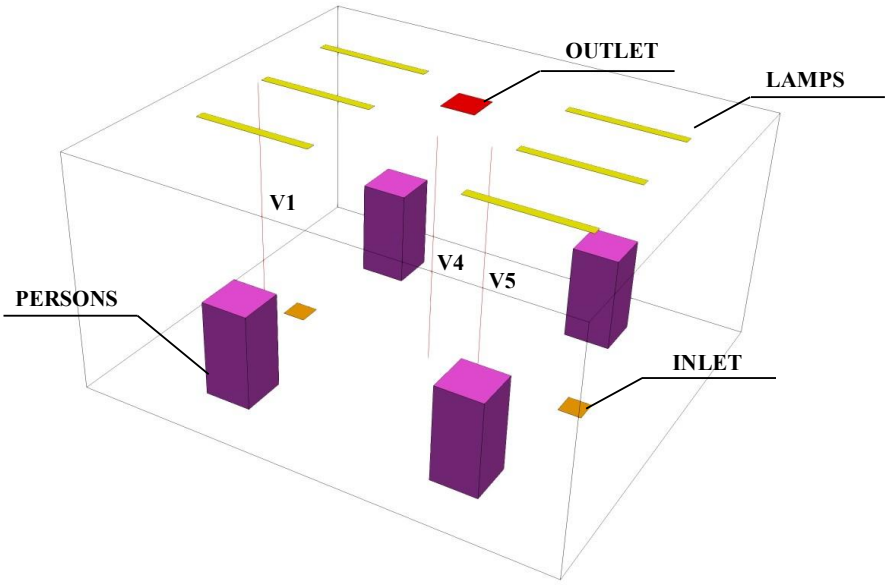


Figure 5.Geometry, line positions, and boundaries model in the reference study of Zhang et al. [26].

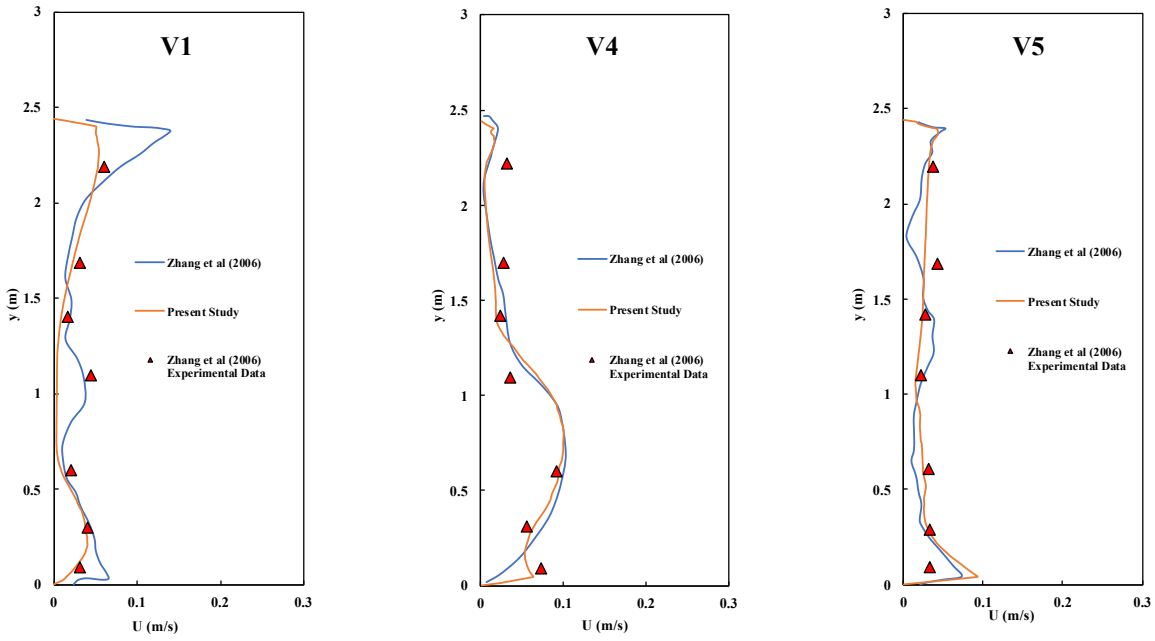


Figure 6.Comparison of the velocity values between the present study and Zhang et al. [26].

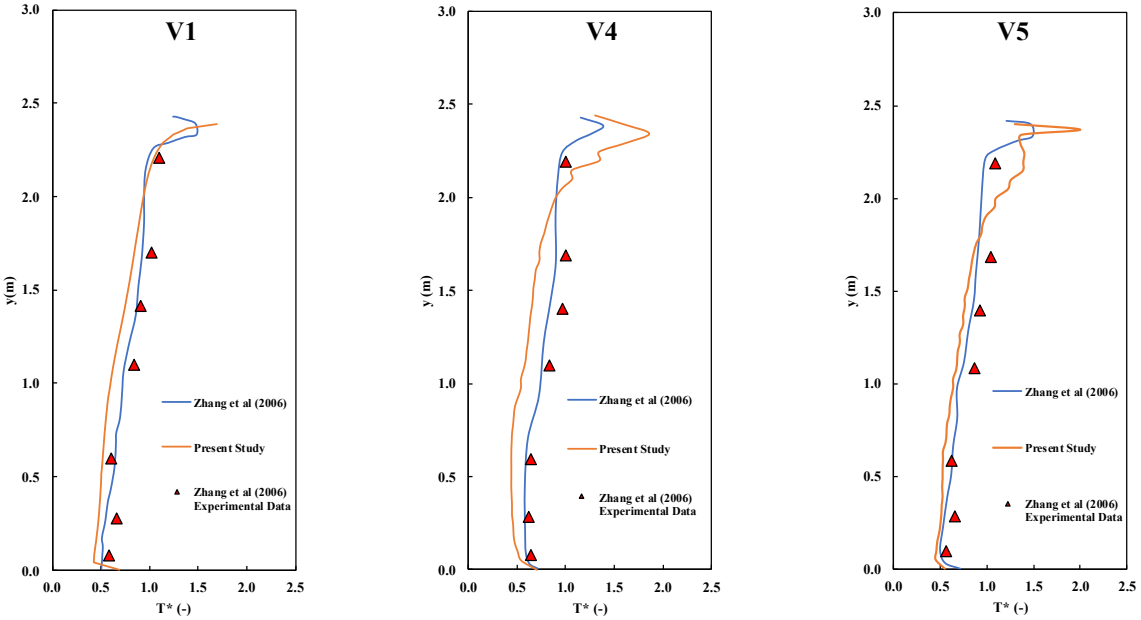


Figure 7.Comparision of temperature between the present study and Zhang et al. [26].

Table 3 reports the Root Mean Squared Error (RMSE) values for temperature and velocity values evaluated along the selected reference lines. The RMSE was computed to quantify the deviation between the present study and reference (experimental or literature) data along the selected lines (V1, V4, and V6). The RMSE is defined in Eq. (13) as:

$$RMSE = \sqrt{\frac{1}{N}\sum\left(\varphi_i^{num} - \varphi_i^{ref}\right)^2} \tag{15}$$

where φ_i^{num} and φ_i^{ref} represent the numerical and reference values (velocity or temperature) at the i-th sampling point, and N is the total number of points along each line. The profiles were sampled at uniformly distributed locations along each line. For temperature, the RMSE was computed using normalized values.

Table 3. RMSE for temperature and Velocity values over selected lines

RMSE	V1	V4	V6
T (-)	0.1568	0.1197	0.0979
u (m/s)	0.0187	0.0187	0.0188

This overall agreement confirms the reliability of the proposed model for the current study.

4.3.2 Particles

The validation of the numerical model was extended to the simulation of respiratory particle dispersion by replicating a well-established reference case from the literature, concerning the emission and dispersion of droplets generated by a coughing event in an indoor environment, Figure 8.

The computational domain and boundary conditions were implemented as in the reference configuration from the study of Liu et al. [34]. On the Eulerian side, the expiratory jet was prescribed at the nozzle as a velocity inlet with a Gaussian radial profile, implemented through a dedicated boundary condition to enforce the target distribution across the inlet patch.

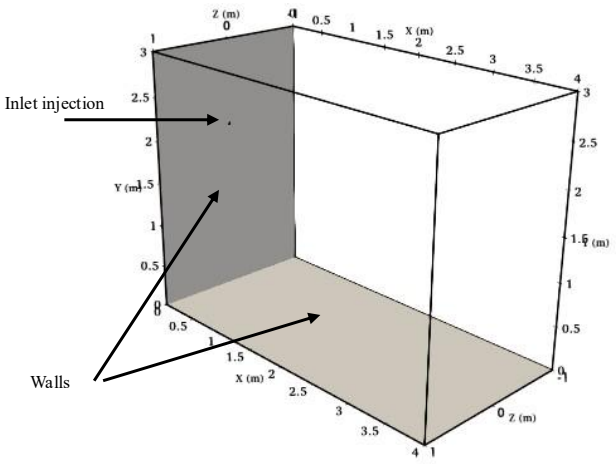


Figure 8.Geometry in the case study of Liu et al. [28]

Ambient air was initialized at 25 °C, while the cough inflow temperature was set to 36 °C; all solid boundaries were treated as no-slip walls.

On the Lagrangian side, particles were injected from the nozzle using a cone injection model, with two representative droplet diameters (60 μm and 100 μm), and a total of 50,000 parcels were released over an injection duration of 500 s, using a transient uncoupled formulation.

Droplet phase-change was neglected (no evaporation), and turbulent dispersion was modelled via the Discrete Random Walk (DRW) approach.[34]

Regarding particle–boundary interaction, openings (and the inlet boundary) were assigned an escape condition (particles leaving the domain are removed), whereas walls were treated as a trap (deposition upon impact).

The comparison between the present study and the experimental data by Liu et al.[34] shows a generally good agreement in terms of particle dispersion patterns for both droplet sizes.

As presented in Figure 9, for larger droplets ($d_{\mathrm{p0}} = 100\ \mu m$), both datasets indicate a limited streamwise travel distance, with particles rapidly settling due to gravitational effects. The present simulation reproduces well the overall deposition region, showing a similar concentration of particles within approximately 1–1.5 m from the source.

For the smaller droplets ($d_{\mathrm{p0}} = 60\ \mu m$), a comparatively wider dispersion is observed, with particles transported further downstream and exhibiting a broader vertical distribution. The present study captures the main transport mechanisms, including the extended streamwise penetration and enhanced dispersion induced by airflow. Although a slightly larger spread is predicted compared to reference study, particularly in the downstream region, the overall trends remain consistent.

These results confirm that the numerical model accurately reproduces the key physical mechanisms governing droplet transport, including the balance among inertial effects, airflow advection, and gravitational settling.

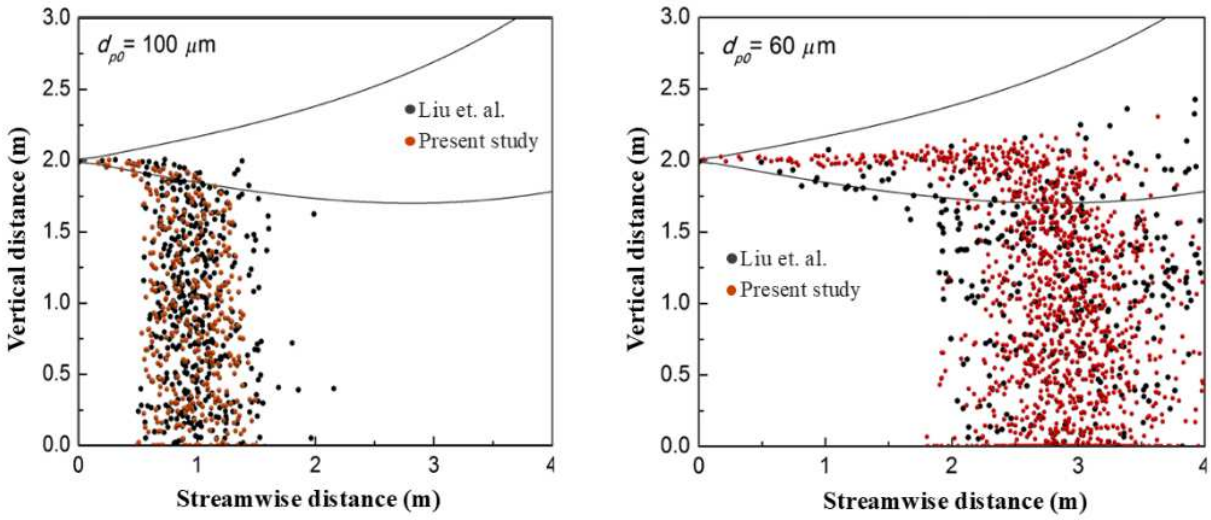


Figure 9.Comparison of particle dispersion in two different sizes with the study of Liu et al. [28]

5 Results and discussion

In this section, the results of the V simulations performed for the investigated indoor environment, with the aim of analysing thermo-fluid dynamic behaviour, particle dispersion and QMRA derived indirect esposure risk indicators under representative operating conditions, have been reported. The analysis considers the distribution of air velocity and temperature fields together with particle transport and deposition patterns derived from the adopted Eulerian–Lagrangian framework.

5.1 Temperature and velocity distribution

After validation of the numerical model, Figure 10, Figure 11 and Figure 12 illustrate the distributions of indoor airflow and temperature as occupancy increases from 25% to overfull conditions. Subfigures (a), (b), (c), and (d) correspond respectively to 25%, 50%, full, and overfull occupancy, allowing a direct comparison of airflow development, recirculation patterns, and thermal stratification within the domain.

Under 25% occupancy case, as illustrated in Figure 10 (a) and Figure 11 (a), the supply jets maintain a coherent structure, penetrating deeper into the occupied zone before interacting with the surrounding air. In that case, recirculation regions remain confined near boundaries and behind seating rows. As depicted in Figure 12 (a), the temperature field shows clearly defined colder regions aligned with the supply airflow, indicating a predominantly momentum-driven regime, in which buoyancy effects from occupants are limited. In this configuration, as shown in Figure 10 (a) airflow velocity gradients are more pronounced near inlets, while the areas far from the inlet grills present stagnation zones.

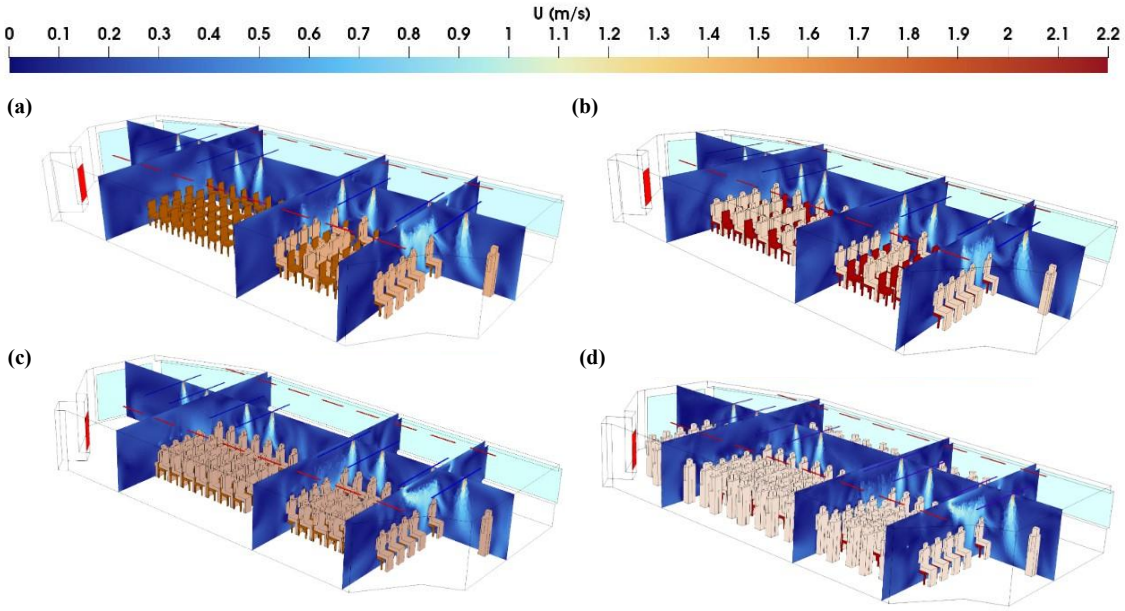


Figure 10.Airflow velocity magnitude distribution on vertical sections under different occupancy scenarios: (a) 25%, (b) 50%, (c) full occupancy, and (d) overfull occupancy.

As occupancy increases to 50% in Figure 10 (b) and Figure 11 (b), the airflow structure progressively evolves. The streamline patterns suggest the formation of localized recirculation zones above the seating area, associated with the interaction between descending airflow and the growing number of thermal plumes generated by occupants. The temperature distribution shows a visible expansion of warmer regions, particularly around seated areas, indicating that buoyancy effects begin to influence the momentum balance. This results in reduced jet penetration and increases lateral spreading, i.e., a wider expansion of the airflow perpendicular to the main jet direction.

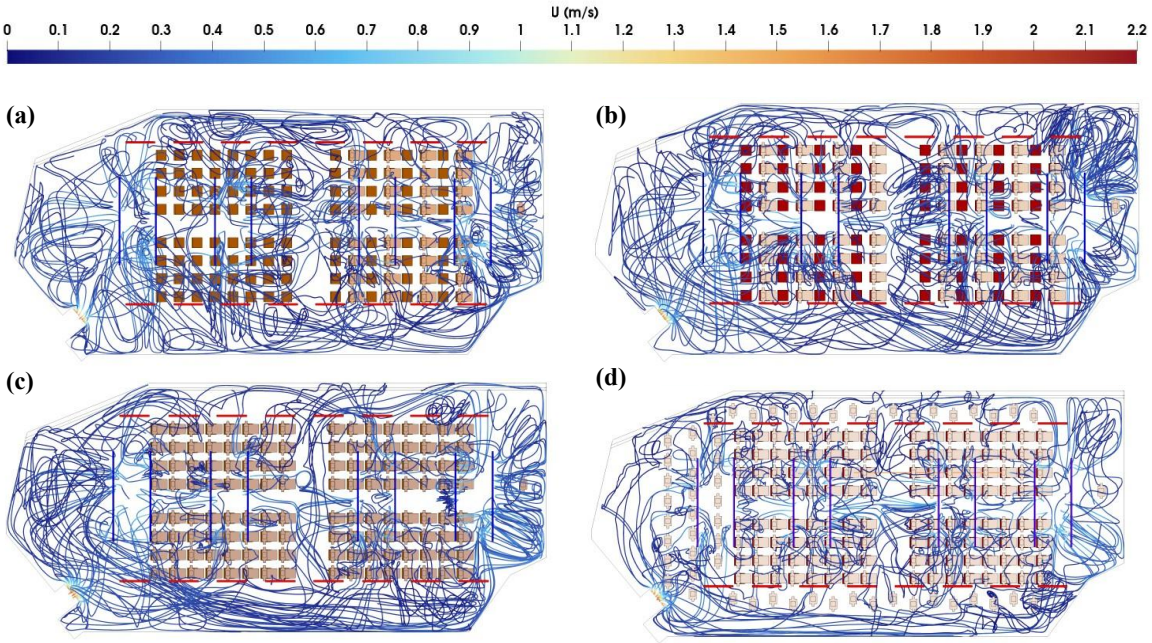


Figure 11.Airflow structure represented by streamline patterns for different occupancy levels: (a) 25%, (b) 50%, (c) full occupancy, and (d) overfull occupancy.

In the full occupancy case, the airflow regime transitions toward a buoyancy-influenced flow. The jets become shorter and less coherent, while recirculation structures expand and merge, as visible in Figure 10 (c) and Figure 11 (c), where low-velocity regions extend across multiple seating rows and along the ceiling. The temperature profile in that case reveal a broader warm layer developing above the occupied region, suggesting that the cumulative heat release alters the vertical airflow structure. The reduced jet momentum prevents direct penetration into the occupied zone, promoting mixing mainly in the upper region of the room and reducing localized airflow effects at the occupant level.

Under overfull occupancy as shown in Figure 10 (d) and Figure 11 (d), the airflow patterns display an interconnected network of recirculation regions extending across the entire seating area. The temperature field becomes more uniformly warm due to the increased endogenous thermal load generated by occupants, with localized colder regions remaining near the supply jets. Individual thermal plumes merge into a buoyancy-driven stratified layer that modifies the hydrostatic pressure distribution and promotes upward motion before air returns along room boundaries. This behaviour indicates a shift from jet-dominated to plume-influenced mixing. A persistent feature across all cases is the presence of a low-velocity region near the presenter, where the standing body acts as an obstruction to the incoming airflow, generating a wake. With increasing occupancy, the cumulative effect of thermal plumes strengthens buoyancy-driven upward motion, reducing the momentum of the supply jet in the front region.

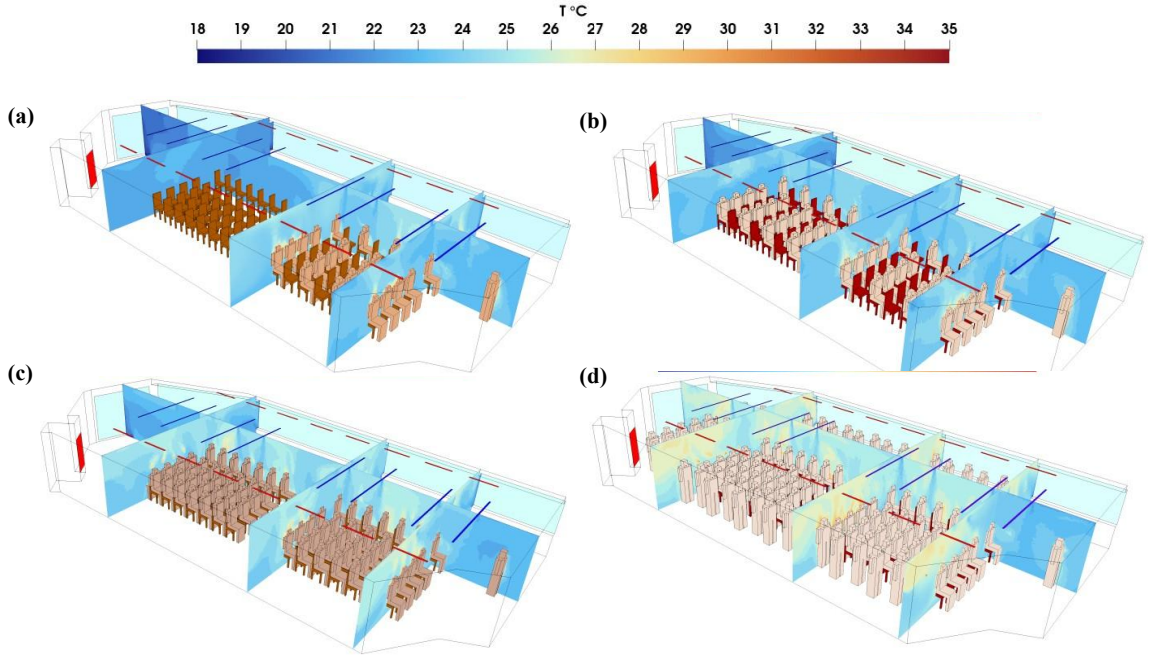


Figure 12.Temperature distribution for different occupancy levels: (a) 25%, (b) 50%, (c) full occupancy, and (d) overfull occupancy.

5.2 Comfort condition

The PMV distributions presented in Figure 13 reflect the combined influence of airflow velocity and temperature evolution described in the previous section. Increasing occupancy leads to higher thermal loads and warmer comfort conditions, while stronger thermal plumes reduce the direct penetration of supply airflow into the

occupied zone. At 25% occupancy Figure 13 (a), PMV values remain closer to slightly cool or neutral conditions, with localized variations beneath the supply jets. These variations correspond to regions of higher comfort and lower temperature identified in the airflow analysis, indicating that air movement near the occupants enhances convective heat transfer, leading to lower perceived thermal sensation.

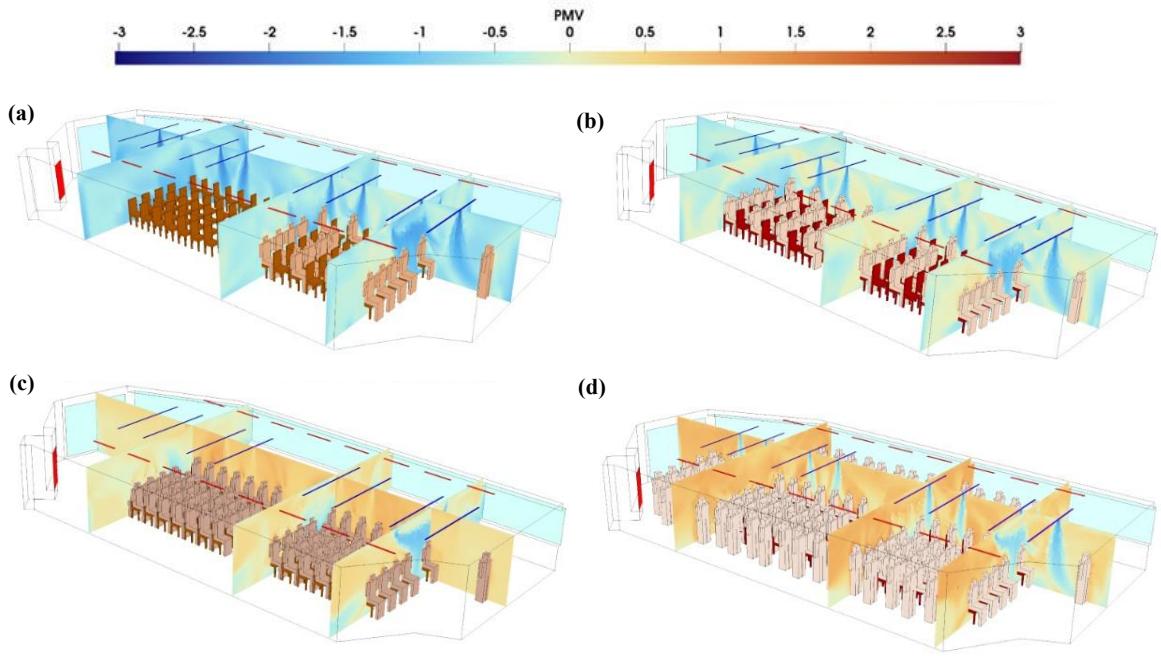


Figure 13.Predicted Mean Vote (PMV) distribution for different occupancy scenarios: (a) 25%, (b) 50%, (c) full occupancy, and (d) overfull occupancy.

With 50% occupancy, PMV values in Figure 13 (b) shift toward neutral conditions. The increase in warmer regions observed in the temperature field reduces local convective heat transfer, while recirculation zones create low-velocity regions where warmer air accumulates, resulting in localized increases in PMV and greater spatial variability in thermal comfort. The coexistence of slightly cooler zones near the jets and warmer areas within seating clusters highlights the heterogeneous nature of the indoor environment.

In the full occupancy scenario, Figure 13 (c), PMV values become more uniformly positive, reflecting the reduced penetration of airflow and the development of a broader warm layer above the audience. The decreased airflow velocity at seated height limits convective heat loss, leading to an increase in PMV values (i.e., a shift toward warmer thermal sensation), despite increased mixing in the upper air.

The overfull occupancy case, Figure 13 (d), represents the most critical condition from a comfort perspective. PMV values increase further and approach warm discomfort conditions, consistent with the collective buoyancy-driven airflow identified in the velocity and temperature analysis. The diminished influence of supply airflow at occupant level reduces the effectiveness of heat distribution, while persistent recirculation zones promote a more homogeneous but warmer indoor environment.

Table 4 reports the PMV values for the investigated cases along rows 1, 3, 5, and 7 highlighting the corresponding comfort conditions. First, there is a trend in the PMV values changing as the occupancy rate increases, moving from slightly cold to slightly warm in all scenarios, reflecting the impact of the number of people in the room. In the 25% occupancy case, an average PMV of −0.5 is observed, indicating that occupants experience slightly cool conditions. This result is consistent with the relatively large size of the room compared to the number of occupants,

which makes the space appear sparsely occupied. This suggests that, under these conditions, the supply air temperature should be increased to achieve thermal neutrality.

In the 50% occupancy case, the average PMV is −0.4, showing a slight increase compared to the previous case. This behavior can be attributed to the increased number of people in the room, that leads to an increase in the air recirculation zones. However, a slight thermal discomfort is still perceived, and an increase in the supply air temperature would also be required in this case to improve comfort conditions.

Under design occupancy (full occupancy case), an average PMV of 0.03 is observed. The room designed for this number of occupants provides overall thermal comfort conditions. The increase in recirculation zones, combined with the contribution of the occupants' internal heat gains, allows the system to compensate for the thermal load not directly covered by the HVAC system.

As the room becomes more crowded, approaching overfull occupancy, the average PMV increases to 0.41. This is due to both the intensification of recirculation zones and the significant increase in internal heat gains from occupants, leading to a rise in indoor air temperature.

Table 4. PMV Comparison in different occupancy scenario.

ROW	OCCUPANCY RATE			
	25%	**50%**	**100%**	**Overfull**
1	-0.5	-0.42	-0.024	0.28
3	-0.38	-0.34	0.18	0.55
5	-0.54	-0.44	0.04	0.42
7	-0.6	-0.43	-0.07	0.4

Figure 14 compares the PMV distribution across chair rows for all occupancy levels. A progressive increase in PMV is observed as occupancy increases, with average values shifting from approximately −0.5 at 25% occupancy to around 0.75 under overfull occupancy.

At 25% occupancy, PMV values remain predominantly negative (between −0.6 and −0.2), indicating slightly cool conditions, with lower values in rows directly exposed to supply airflow. Increasing occupancy to 50% moves PMV closer to neutral (−0.2 to 0.2), while still showing spatial variability between rows. At full occupancy, PMV is mostly positive (≈ 0.2–0.5), reflecting increased internal heat gains and reduced local cooling. The highest values occur at overfull occupancy, where PMV approaches warm discomfort levels (up to 0.75), with reduced variability across rows compared to lower-occupancy cases.

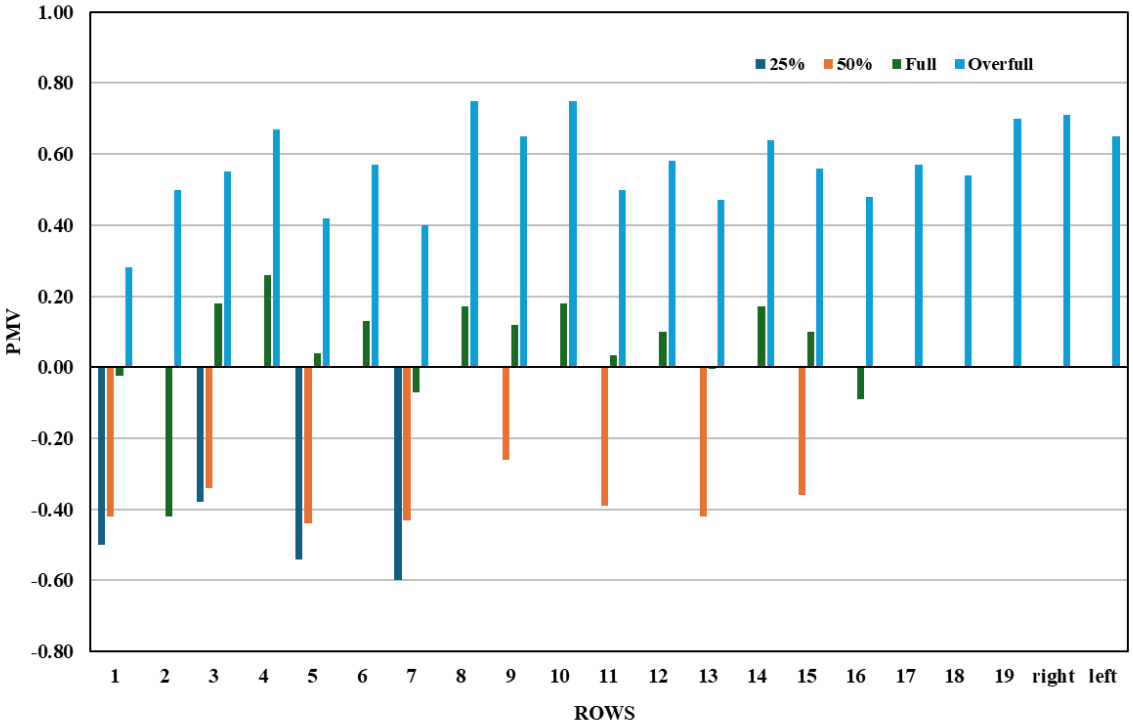
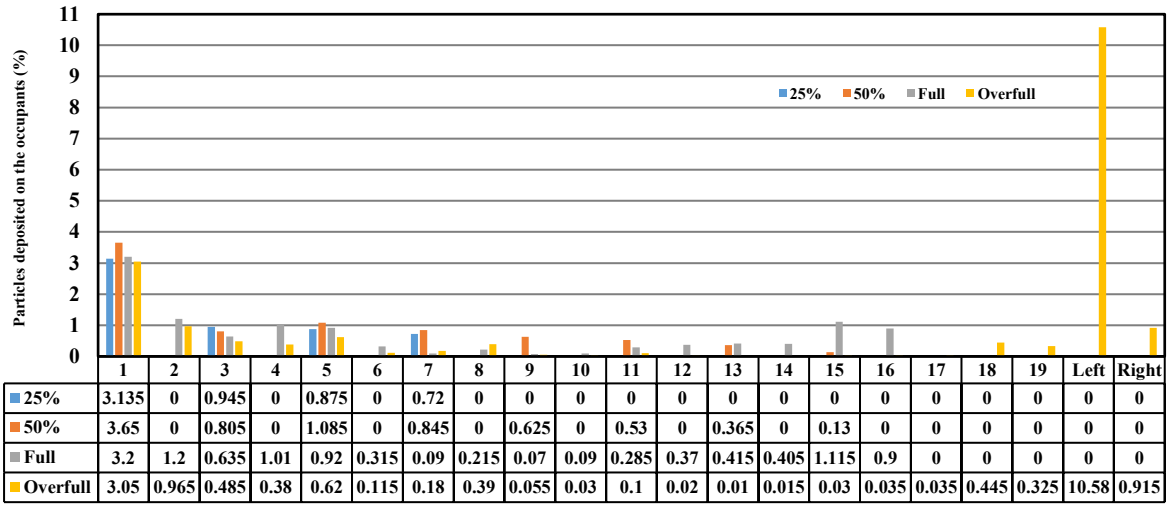


Figure 14.Row-averaged PMV values in different occupancy scenarios for the seating rows of the conference room.

Moreover, it is worth mentioning that in all cases, the presenter area emerges as a localized critical zone, where wake formation and a strong thermal plume generate noticeable local variations in PMV.

5.3 Particle distribution and infection risk

The particulate analysis shows that, across all investigated scenarios, most particles emitted by the presenter deposit along the first row of occupants, as presented in Figure 15. A clear spatial asymmetry is observed, with a predominant deposition on the right-hand side of the room, i.e., the side without windows, as shown in Figure 16. This behavior is attributed to the airflow field, which is mainly directed toward the largest outlet located at the rear of the room.



	1	2	3	4	5	6	7	8	9	10	11	12	13	14	15	16	17	18	19	Left	Right
25%	3.135	0	0.945	0	0.875	0	0.72	0	0	0	0	0	0	0	0	0	0	0	0	0	0
50%	3.65	0	0.805	0	1.085	0	0.845	0	0.625	0	0.53	0	0.365	0	0.13	0	0	0	0	0	0
Full	3.2	1.2	0.635	1.01	0.92	0.315	0.09	0.215	0.07	0.09	0.285	0.37	0.415	0.405	1.115	0.9	0	0	0	0	0
Overfull	3.05	0.965	0.485	0.38	0.62	0.115	0.18	0.39	0.055	0.03	0.1	0.02	0.01	0.015	0.03	0.035	0.035	0.445	0.325	10.58	0.915

ROWS

Figure 15.Row-wise distribution of particle deposition on occupants expressed as percentage of total deposited particles under different occupancy scenarios (25%, 50%, Full, and Overfull)

Considering all scenarios, approximately 3.25% of the particles emitted by the presenter deposit on the first row on average. This result is consistent with the position of the emission source, namely the presenter, who is located a few meters from this area. As the distance from the source increases, the percentage of deposited particles in subsequent rows progressively decreases, from an average of about 1.08% in the second row to 0.71% in the third and approaches zero in the last rows.

In partially occupied configurations (25% and 50% cases), it is also observed that the percentage of deposited particles along unoccupied rows is zero. This is due to the absence of significant recirculation zones in these regions, which prevents particles from reaching and remaining in those areas.

In the overfull occupancy scenario, Figure 16 (d), the most critical condition is observed in the standing row located on the left-hand side of the room, opposite to the row near the windows. In this area, particle deposition reaches approximately 10.58%, as reported in Figure 15. This result is consistent with the prevailing airflow direction toward the main outlet and with the combined effect of the internal heat gains generated by occupants. These increments in air recirculation promote particle transport; as a result, particles tend to remain suspended rather than depositing on the floor, ultimately adhering to the surfaces of standing occupants.

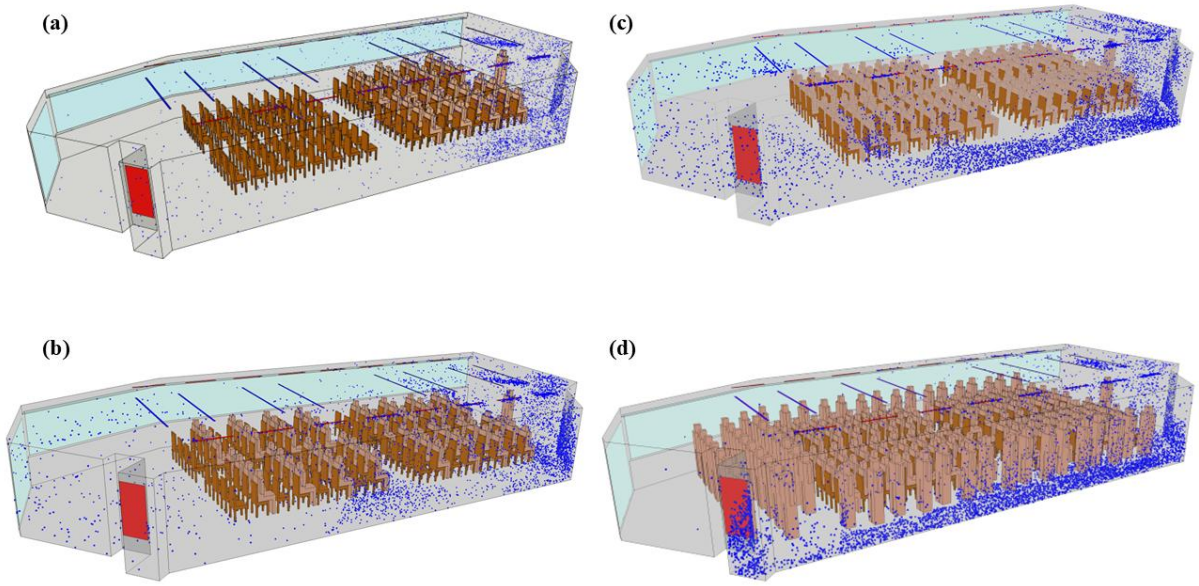
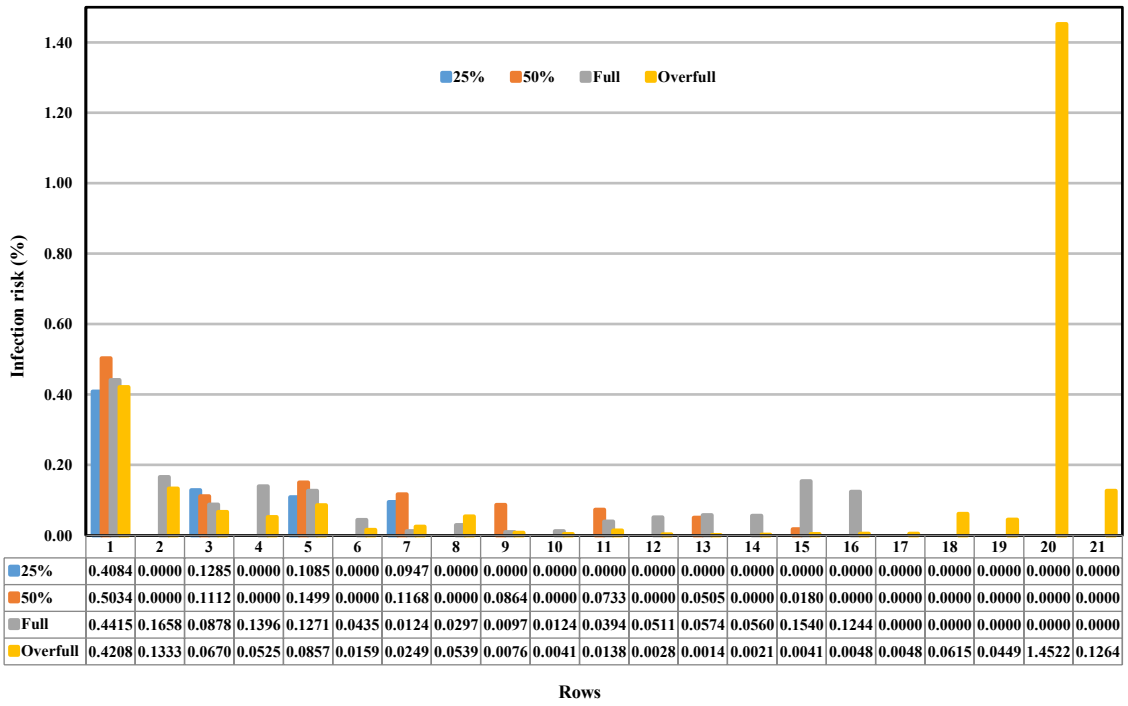


Figure 16.Three-dimensional visualization of Lagrangian particle dispersion within the conference room under different occupancy scenarios: (a) 25% occupancy, (b) 50% occupancy, (c) full occupancy, and (d) overfull occupancy.

The QMRA-based indirect exposure analysis, shown in Figure 17, closely follows the spatial patterns observed in particle deposition, confirming the strong dependence of exposure on airflow-driven transport mechanisms. This consistency is expected, as the adopted infection model directly links the probability of infection to the number of particles that reach and deposit on occupants.

The first seating row consistently emerges as the most exposed region, with an average exposure risk of 0.44%, due to its proximity to the emission source. Under overfull occupancy conditions, the highest risk is observed among standing occupants located on the right-hand side of the room, where values reach up to 1.45%. This critical behavior is driven by the dominant airflow pathway connecting the emission source to the main outlet, which effectively channels particles along preferential trajectories. These findings emphasize the need to avoid occupant positioning along primary airflow paths, particularly in high-density conditions.



	1	2	3	4	5	6	7	8	9	10	11	12	13	14	15	16	17	18	19	20	21
25%	0.4084	0.0000	0.1285	0.0000	0.1085	0.0000	0.0947	0.0000	0.0000	0.0000	0.0000	0.0000	0.0000	0.0000	0.0000	0.0000	0.0000	0.0000	0.0000	0.0000	0.0000
50%	0.5034	0.0000	0.1112	0.0000	0.1499	0.0000	0.1168	0.0000	0.0864	0.0000	0.0733	0.0000	0.0505	0.0000	0.0180	0.0000	0.0000	0.0000	0.0000	0.0000	0.0000
Full	0.4415	0.1658	0.0878	0.1396	0.1271	0.0435	0.0124	0.0297	0.0097	0.0124	0.0394	0.0511	0.0574	0.0560	0.1540	0.1244	0.0000	0.0000	0.0000	0.0000	0.0000
Overfull	0.4208	0.1333	0.0670	0.0525	0.0857	0.0159	0.0249	0.0539	0.0076	0.0041	0.0138	0.0028	0.0014	0.0021	0.0041	0.0048	0.0048	0.0615	0.0449	1.4522	0.1264

Rows

Figure 17.Estimated fomite-mediated infection risk (%) for each seating row under different occupancy levels (25%, 50%, 100%, and overfull), derived from QMRA analysis based on particle deposition results.

A notable trade-off between thermal comfort and indoor air quality is also identified. As occupancy increases, the PMV progressively shifts toward neutral or slightly warm conditions due to an increase in internal heat gains, while airflow velocities at the occupant level decrease. This reduction in local air movement limits particle removal and promotes accumulation within the occupied zone, thereby increasing infection risk.

Specifically, at 25% occupancy, the average PMV in the first row is around −0.5, corresponding to slightly cool conditions, while infection risk remains below 0.5% due to effective dilution. At 50% occupancy, PMV improves toward −0.4; however, this is accompanied by a rise in infection risk (≈0.5%), highlighting the reduced ventilation effectiveness. The full occupancy case represents the optimal balance, with near-neutral PMV (≈0) and moderate infection risk slightly above 0.4%. In contrast, under overfull conditions, the thermal environment shifts toward warm discomfort (PMV ≈ 0.41), while infection risk decreases again to below 0.5% in seated areas, likely due to enhanced buoyancy-driven mixing and particle redistribution.

Overall, the results suggest that increasing occupancy not only alters thermal comfort but also fundamentally modifies airflow structure, with direct implications for airborne exposure. These findings highlight the importance of integrated HVAC control strategies that simultaneously address thermal comfort and multiple pathogen transmission pathways, rather than focusing exclusively on airborne transmission.

6 Conclusions

In this study, an integrated CFD coupled with a quantitative microbial risk assessment framework based on a steady RANS airflow solution coupled with Lagrangian particle tracking was applied to investigate thermo-fluid dynamic behaviour, particle dispersion, and infection-risk distribution under different occupancy scenarios. To clearly highlight the main outcomes, the key findings of the present study are summarized as follows:

- Airflow, thermal comfort, and occupancy

  Increasing occupancy progressively reduces airflow velocity in the occupied zone due to enhanced buoyancy effects and greater flow obstruction caused by occupants. As a result, thermal comfort deteriorates, with the PMV shifting from slightly cool conditions (≈ -0.5) at 25% occupancy to warm discomfort levels ($\approx +0.75$) under overfull conditions because of increased internal heat gains and the interaction between occupant thermal plumes and the ventilation airflow.
- Particle transport and infection risk

  Particle dispersion is primarily governed by the ventilation airflow organization. The first seating row consistently experiences the highest deposition and exposure because it directly intercepts the respiratory plume before significant dilution occurs. As occupancy increases, stronger recirculation and entrainment mechanisms produce a more heterogeneous particle distribution, leading to higher infection risk, with QMRA values reaching approximately 0.44% for seated occupants and up to 1.45% for standing occupants under overfull conditions.
- Relationship between airflow and contaminant exposure

  The results demonstrate that indirect infection risk depends mainly on airflow organization—including ventilation jets, buoyancy-driven flows, and recirculation zones—rather than on geometric distance from the emission source alone. A clear trade-off also emerges between thermal comfort and indoor air quality: conditions closer to thermal neutrality (PMV ≈ 0) are associated with lower airflow velocities and longer particle residence times, whereas slightly cooler conditions promote stronger air circulation and more effective particle removal.

Overall, this study advances a multidisciplinary assessment framework that integrates CFD-based airflow analysis with health-oriented indicators, highlighting the need for design methodologies capable of simultaneously addressing comfort, ventilation effectiveness, and exposure mitigation.

Some limitations of the present study should be acknowledged. The airflow field was simulated using a steady-state RANS approach, and occupant movements were not considered. The Lagrangian particle-tracking model assumed a single particle size and neglected evaporation, breakup, coalescence, and particle resuspension. Furthermore, only mechanically ventilated conditions were investigated. The adopted QMRA framework was used to derive comparative risk indicators associated with the hand–fomite–mucosa transmission pathway and should not be interpreted as a comprehensive estimate of airborne infection probability. Finally, several QMRA parameters, including viral load, transfer efficiencies, contact frequencies, and viral decay rates, are affected by uncertainty; therefore, the results should be interpreted primarily as relative indicators for comparing occupancy scenarios.

Data availability statement

Some or all data, models, or codes that support the findings of this study are available from the corresponding author upon reasonable request.

Funding

This research received no external funding.

Clinical Trial Registration

Not applicable. This study is based on computational fluid dynamics (CFD) simulations and numerical assessments of indoor environmental conditions and airborne particle transport. No clinical trials or interventional studies involving human participants were conducted.

References

[1] Zabihi M, Li R, Brinkerhoff J. A novel aerosol induction-removal system for mitigating airborne disease transmission in shared indoor environments. Build Environ 2025;286. https://doi.org/10.1016/j.buildenv.2025.113569.

[2] Ting JZC, Sia CCV, Yeu EYL, Chung PP, Thangavelu SK, Joseph AA. Correlation of experimental data and simulation models in adaptive thermal comfort analysis for university classrooms. Energy Build 2025;349. https://doi.org/10.1016/j.enbuild.2025.116561.

[3] Chang L, Permana I, Setiawan T, Agharid AP, Wang F. Evaluating and enhancing thermal comfort and indoor air quality in a library building through measurement and simulation. Ain Shams Engineering Journal 2025;16. https://doi.org/10.1016/j.asej.2025.103580.

[4] Zhuang R, Li X, Tu J. CFD study of the effects of furniture layout on indoor air quality under typical office ventilation schemes. Build Simul 2014;7:263–75. https://doi.org/10.1007/s12273-013-0144-5.

[5] Yang L, Ye M, he BJ. CFD simulation research on residential indoor air quality. Science of The Total Environment 2014;472:1137–44. https://doi.org/10.1016/J.SCITOTENV.2013.11.118.

[6] Daisey JM, Angell WJ, Apte MG. Indoor air quality, ventilation and health symptoms in schools: an analysis of existing information. Indoor Air 2003;13:53–64. https://doi.org/10.1034/J.1600-0668.2003.00153.X.

[7] Finnegan MJ, Pickering CAC, Burge PS. The sick building syndrome: prevalence studies. Br Med J (Clin Res Ed) 1984;289:1573–5. https://doi.org/10.1136/BMJ.289.6458.1573.

[8] Jurelionis A, Isevičius E. CFD predictions of indoor air movement induced by cold window surfaces. Journal of Civil Engineering and Management 2008;14:29–38. https://doi.org/10.3846/1392-3730.2008.14.29-38.

[9] Ramponi R, Blocken B. CFD simulation of cross-ventilation for a generic isolated building: Impact of computational parameters. Build Environ 2012;53:34–48. https://doi.org/10.1016/J.BUILDENV.2012.01.004.

[10] Nag PK. Sick Building Syndrome and Other Building-Related Illnesses. Office Buildings 2018:53. https://doi.org/10.1007/978-981-13-2577-9_3.

[11] Siddiqui M, Jayanti S, Swaminathan T. CFD analysis of dense gas dispersion in indoor environment for risk assessment and risk mitigation. J Hazard Mater 2012;209–210:177–85. https://doi.org/10.1016/j.jhazmat.2012.01.007.

[12] Huizenga C, Abbaszadeh S, Zagreus L, Arens E. Air quality and thermal comfort in office buildings: results of a large indoor environmental quality survey 2006.

[13] Kovesi T, Creery D, Gilbert NL, Dales R, Fugler D, Thompson B, et al. Indoor air quality risk factors for severe lower respiratory tract infections in Inuit infants in Baffin Region, Nunavut: A pilot study. Indoor Air 2006;16:266–75. https://doi.org/10.1111/J.1600-0668.2006.00423.X;WGROUP:STRING:PUBLICATION.

[14] Yu T; ;, Liu P;, Li X, Li T, Fan X, Yu T, et al. Uniformity of Supply Air in the Plenum for Under-Floor Air Distribution Ventilation in a Circular Conference Room: A CFD Study. Energies 2022, Vol 15, Page 6370 2022;15:6370. https://doi.org/10.3390/EN15176370.

[15] Maury-Micolier A, Huang L, Jolliet O. Coupled mass and heat transfer modelling in building envelopes to consistently assess human exposure and energy performance in indoor environments. J Build Perform Simul 2023;16:734–48. https://doi.org/10.1080/19401493.2023.2200377.

[16] Atthajariyakul S, Leephakpreeda T. Real-time determination of optimal indoor-air condition for thermal comfort, air quality and efficient energy usage. Energy Build 2004;36:720–33. https://doi.org/10.1016/J.ENBUILD.2004.01.017.

[17] D'Alicandro AC, Capozzoli A, Mauro A. Thermofluid dynamics and droplets transport inside a large university classroom: Effects of occupancy rate and volumetric airflow. J Aerosol Sci 2024;175:106285. https://doi.org/10.1016/J.JAEROSCI.2023.106285.

[18] Nada SA, El-Batsh HM, Elattar HF, Ali NM. CFD investigation of airflow pattern, temperature distribution and thermal comfort of UFAD system for theater buildings applications. Journal of Building Engineering 2016;6:274–300. https://doi.org/10.1016/J.JOBE.2016.04.008.

[19] Jahromi RH, Fraia S Di, … NM-A at S. Hygrothermal Comfort and Indoor Air Quality in Train Cabins: Assessing the Effect of Hvac Configuration and Operation. PapersSsrnComR Hamidi Jahromi, S Di Fraia, N Massarotti, A MauroAvailable at SSRN 5356356•papersSsrnCom n.d. https://doi.org/https://doi.org/10.1016/j.jaerosci.2025.106720.

[20] Massarotti N, Mauro A, Sainas D, Marinetti S, Rossetti A. CFD modelling of an operating theater. International Symposium on Advances in Computational Heat Transfer 2017:881–4. https://doi.org/10.1615/ichmt.2017.cht-7.890.

[21] Nada SA, Said MA, Rady MA. Numerical investigation and parametric study for thermal and energy management enhancements in data centers' buildings. Appl Therm Eng 2016;98:110–28. https://doi.org/10.1016/j.applthermaleng.2015.12.020.

[22] Lee H, Rim D. Assessment of airborne transmitted infection risk in classrooms using computational fluid dynamics and machine learning-based surrogate modeling. Journal of Building Engineering 2024;97:110760. https://doi.org/10.1016/J.JOBE.2024.110760.

[23] Bhagat RK, Davies Wykes MS, Dalziel SB, Linden PF. Effects of ventilation on the indoor spread of COVID-19. J Fluid Mech 2020;903:F1. https://doi.org/10.1017/JFM.2020.720.

[24] Li Y, Leung GM, Tang JW, Yang X, Chao CYH, Lin JZ, et al. Role of ventilation in airborne transmission of infectious agents in the built environment - A multidisciplinary systematic review. Indoor Air 2007;17:2–18. https://doi.org/10.1111/J.1600-0668.2006.00445.X;JOURNAL:JOURNAL:16000668;WGROUP:STRING:PUBLICATION.

[25] Vita G, Woolf D, Avery-Hickmott T, Rowsell R. A CFD-based framework to assess airborne infection risk in buildings. Build Environ 2023;233:110099. https://doi.org/10.1016/J.BUILDENV.2023.110099.

[26] Moeller L, Wallburg F, Kaule F, Schoenfelder S. Numerical Flow Simulation on the Virus Spread of SARS-CoV-2 Due to Airborne Transmission in a Classroom. International Journal of Environmental Research and Public Health 2022, Vol 19, Page 6279 2022;19:6279. https://doi.org/10.3390/IJERPH19106279.

[27] Buonanno G, Ricolfi L, Morawska L, Stabile L. Increasing ventilation reduces SARS-CoV-2 airborne transmission in schools: A retrospective cohort study in Italy's Marche region. Front Public Health 2022;10:1087087. https://doi.org/10.3389/FPUBH.2022.1087087/TEXT.

[28] Mariam, Magar A, Joshi M, Rajagopal PS, Khan A, Rao MM, et al. CFD Simulation of the Airborne Transmission of COVID-19 Vectors Emitted during Respiratory Mechanisms: Revisiting the Concept of Safe Distance. ACS Omega

2021;6:16876–89. https://doi.org/10.1021/ACSOMEGA.1C01489/SUPPL_FILE/AO1C01489_SI_003.MP4.

[29] Carducci A, Donzelli G, Cioni L, Verani M. Quantitative Microbial Risk Assessment in Occupational Settings Applied to the Airborne Human Adenovirus Infection. International Journal of Environmental Research and Public Health 2016, Vol 13, Page 733 2016;13:733. https://doi.org/10.3390/IJERPH13070733.

[30] Arpino F, Cortellessa G, D'Alicandro AC, Grossi G, Massarotti N, Mauro A. CFD analysis of the air supply rate influence on the aerosol dispersion in a university lecture room. Build Environ 2023;235. https://doi.org/10.1016/J.BUILDENV.2023.110257.

[31] Taha TR. An Introduction to Parallel Computational Fluid Dynamics. IEEE Concurrency 2005;6:78–78. https://doi.org/10.1109/mcc.1998.736434.

[32] Zhang Z, Chen Q. Experimental measurements and numerical simulations of particle transport and distribution in ventilated rooms. Atmos Environ 2006;40:3396–408. https://doi.org/10.1016/J.ATMOSENV.2006.01.014.

[33] Jahromi RH, Di Fraia S, Massarotti N, Mauro A. On the effect of HVAC recirculation on thermal comfort and indoor air quality in train cabins. J Aerosol Sci 2026;191. https://doi.org/10.1016/j.jaerosci.2025.106720.

[34] Liu L, Wei J, Li Y, Ooi A. Evaporation and dispersion of respiratory droplets from coughing. Indoor Air 2017;27:179–90. https://doi.org/10.1111/INA.12297.

[35] van Beest MRRS, Arpino F, Hlinka O, Sauret E, van Beest NRTP, Humphries RS, et al. Influence of indoor airflow on particle spread of a single breath and cough in enclosures: Does opening a window really 'help'? Atmos Pollut Res 2022;13. https://doi.org/10.1016/j.apr.2022.101473.

[36] Arpino F, Cortellessa G, Grossi G, Nagano H. A Eulerian-Lagrangian approach for the non-isothermal and transient CFD analysis of the aerosol airborne dispersion in a car cabin. Build Environ 2022;209:108648. https://doi.org/10.1016/J.BUILDENV.2021.108648.

[37] ISO 7730:2025 - Ergonomics of the thermal environment — Analytical determination and interpretation of thermal comfort using calculation of the PMV and PPD indices and local thermal comfort criteria n.d.

[38] Wilson AM, Weir MH, Bloomfield SF, Scott EA, Reynolds KA. Modeling COVID-19 infection risks for a single hand-to-fomite scenario and potential risk

reductions offered by surface disinfection. Am J Infect Control 2020;49:846. https://doi.org/10.1016/j.ajic.2020.11.013.

[39] Gammaitoni L, Nucci MC. Using a Mathematical Model to Evaluate the Efficacy of TB Control Measures. Emerg Infect Dis 1997;3:335–42. https://doi.org/10.3201/eid0303.970310.

[40] Despres HW, Mills MG, Shirley DJ, Schmidt MM, Huang M-L, Jerome KR, et al. Quantitative measurement of infectious virus in SARS-CoV-2 Alpha, Delta and Epsilon variants reveals higher infectivity (viral titer:RNA ratio) in clinical samples containing the Delta and Epsilon variants. MedRxiv 2021:2021.09.07.21263229. https://doi.org/10.1101/2021.09.07.21263229.

[41] Pitol AK, Venkatesan S, Richards S, Hoptroff M, Majumdar A, Hughes GL. SARS-CoV-2 survival on skin and its transfer from contaminated surfaces. PLoS One 2025;20:e0325235. https://doi.org/10.1371/journal.pone.0325235.

[42] Kwok YLA, Gralton J, McLaws ML. Face touching: A frequent habit that has implications for hand hygiene. Am J Infect Control 2015;43:112–4. https://doi.org/10.1016/j.ajic.2014.10.015.

[43] Rusin P, Maxwell S, Gerba C. Comparative surface-to-hand and fingertip-to-mouth transfer efficiency of gram-positive bacteria, gram-negative bacteria, and phage. J Appl Microbiol 2002;93:585–92. https://doi.org/10.1046/j.1365-2672.2002.01734.x.

[44] Pitol AK, Julian TR. Community Transmission of SARS-CoV-2 by Surfaces: Risks and Risk Reduction Strategies. Environ Sci Technol Lett 2021;8:263–9. https://doi.org/10.1021/acs.estlett.0c00966.

[45] Miller D, King MF, Nally J, Drodge JR, Reeves GI, Bate AM, et al. Modeling the factors that influence exposure to SARS-CoV-2 on a subway train carriage. Indoor Air 2022;32:e12976. https://doi.org/10.1111/INA.12976;ISSUE:ISSUE:DOI.

[46] Wilson AM, Jones RM. Exploring spatial averaging of contamination in fomite microbial transfer models and implications for dose. Journal of Exposure Science & Environmental Epidemiology 2021 32:5 2021;32:759–66. https://doi.org/10.1038/s41370-021-00398-2.

[47] Watanabe T, Bartrand TA, Weir MH, Omura T, Haas CN. Development of a dose-response model for SARS coronavirus. Risk Analysis 2010;30:1129–38. https://doi.org/10.1111/j.1539-6924.2010.01427.x.

[48] Banholzer N, Middelkoop K, Leukes J, Weingartner E, Schmutz R, Zürcher K, et al. Estimating Mycobacterium tuberculosis transmission in a South African clinic: Spatiotemporal model based on person movements. PLoS Comput Biol 2025;21:e1012823. https://doi.org/10.1371/journal.pcbi.1012823.

[49] UNI EN 1745:2020 - UNI Ente Italiano di Normazione n.d.

[50] UNI 10351:2021 -Building materials - Thermo-hygrometric proprieties - Procedure for determining the design values n.d.

[51] UNI/TS 11300-1:2014 - Ergonomics of thermal environments - Analytical determination and interpretation of thermal comfort through the calculation of PMV and PPD indices and local thermal comfort criteria. n.d.

[52] UNI EN ISO 10456:2008 - UNI Ente Italiano di Normazione n.d.